Applied Physics Letters ARTICLE scitation.org/journal/apl

Enhanced operating temperature in terahertz quantum cascade lasers based on direct phonon depopulation

Cite as: Appl. Phys. Lett. **122**, 161101 (2023); doi: 10.1063/5.0144705
Submitted: 13 February 2023 · Accepted: 3 April 2023 ·
Published Online: 17 April 2023

Ali Khalatpour,[1,a)] Man Chun Tam,[2] Sadhvikas J. Addamane,[3] John Reno,[3] Zbignew Wasilewski,[2] and Qing Hu[1,a)]

AFFILIATIONS

[1]Department of Electrical Engineering and Research Laboratory of Electronics, Massachusetts Institute of Technology, Cambridge, Massachusetts 02139, USA
[2]Department of Electrical and Computer Engineering, University of Waterloo, 200 University Ave W, Waterloo, Ontario N2L 3G1, Canada
[3]Sandia National Laboratories, Center of Integrated Nanotechnologies, Albuquerque, New Mexico 87185-130, USA

[a)]**Authors to whom correspondence should be addressed:** akhalatpour@g.harvard.edu and qhu@mit.edu

ABSTRACT

Room temperature operation of terahertz quantum cascade lasers (THz QCLs) has been a long-pursued goal to realize compact semiconductor THz sources. In this paper, we report on improving the maximum operating temperature of THz QCLs to ∼ 261 K as a step toward the realization of this goal.

The THz spectral range (0.5–10 THz) lies in the gap between frequency ranges accessible with conventional semiconductor electronic and photonic devices. At the lower end of the THz gap, frequency multipliers using electronic devices have reached ∼1.6 THz with milliwatt (mW) optical power at room temperature.[1,2] Both quantum cascade laser-pumped molecular lasers (QPMLs)[3] and difference-frequency generation (DFG)[4,5] have used infrared quantum cascade lasers (IR QCLs) to generate THz waves at room temperature indirectly. Quantum cascade lasers (QCLs) have several advantages compared to the nonlinear frequency upconversion and downconversion schemes. As fundamental oscillators, THz QCLs inherently have much higher power levels and efficiencies than nonlinear frequency conversions. At cryogenic temperatures, THz QCL systems can reach watt-level optical power in pulse mode[6–8] and tens of milliwatts in continuous wave operation with ∼1% efficiency.[9,10] In addition, THz QCL gain medium can be used to develop THz sources, such as frequency combs[11,12] and radiation amplifiers.[13] Another advantage of THz QCLs is that they enable cavities with unique radiation properties. For instance, the local oscillator at 4.74 THz for GUSTO,[14] which is a NASA balloon-borne mission, has been developed using a tunable unidirectional cavity that achieves ∼10 mW of CW power with less than 1.8 W dissipated power, and it is cooled with a compact Stirling cooler (CryoTel®CT) weighing as little as 5 kg.[15] The required size for cooling and the system's vibration will be significantly reduced by using thermoelectric (TE) coolers. Compact, hand-held, TE-cooled THz QCLs were made possible by a record high operating temperature of $T_{max} \sim 250$ K.[16] Here, we report on further improvement to the maximum operating temperature $T_{max} \sim 261$ K.

Figure 1(a) shows a schematic of a three-level laser to illustrate the dominant scattering processes in THz QCLs.[17] Here, the upper lasing level, the lower lasing level, and the ground states in the nth module are denoted by $|u_n\rangle$, $|l_n\rangle$, and $|g_n\rangle$, respectively. *IFR*, *imp*, *e–e*, LO_{em}, and LO_{abs} represent interface roughness scattering, impurity scattering, electron–electron scattering, *LO*-phonon emission, and *LO*-phonon absorption, respectively. In this scheme, electrons are injected into $|u_n\rangle$ and extracted from $|l_n\rangle$ through resonant tunneling and scattering with *LO*-phonons in the heterostructure. The peak gain of intersubband transitions G_p can be described by the oscillator strength f_{ul}, the population inversion between the upper and the lower lasing level ΔN, and the transition linewidth $\Delta\nu$ as $G_p \propto \frac{\Delta N f_{ul}}{\Delta\nu}$. The linewidth is defined as $\Delta\nu = \frac{1}{2\pi}\left(\frac{1}{\tau^u} + \frac{1}{\tau^l} + \frac{2}{T^*}\right)$ in which τ^u, τ^l, and T^* are the

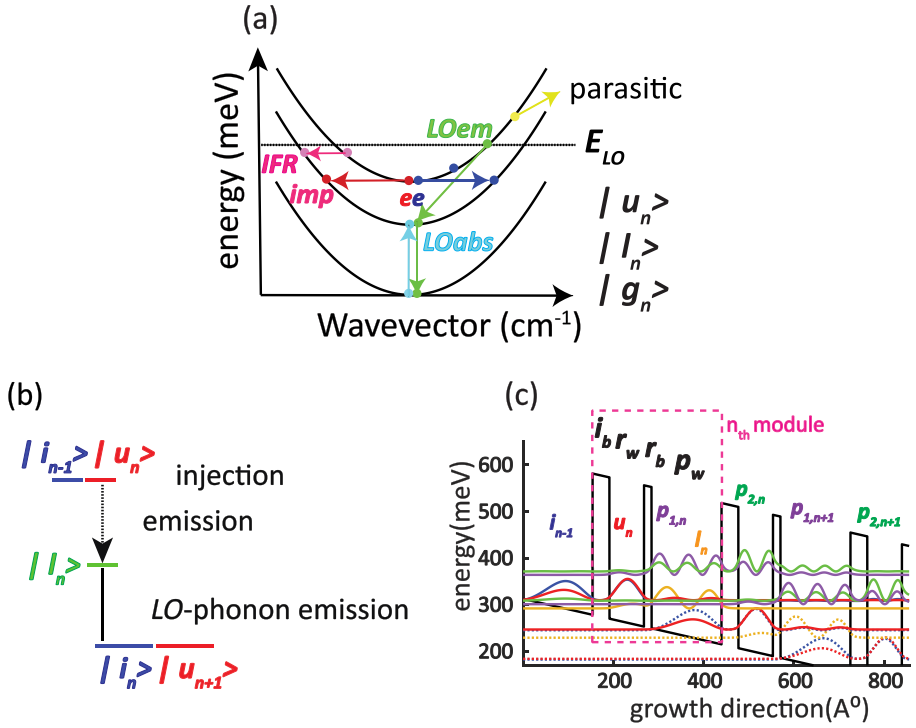

FIG. 1. (a) Schematic of a three-level QCL system. (b) A simple schematic of energy levels in a THz QCLs based on the direct phonon depopulations. (c) Probability density functions of subband states in a THz QCL with a two-wells scheme.

upper-state lifetime, the lower-state lifetime, and pure dephasing times. The oscillator strength is essentially a wavefunction overlap integral between the upper and lower lasing levels and is defined as $f_{ul} = \left(\frac{2m^*\Delta_E}{\hbar^2}\right)|\langle u|z|l\rangle|^2$, in which z is the growth direction, m^* is the effective mass, and Δ_E is the energy separation between the two levels. The explicit temperature dependence of ΔN arises from thermally activated, non-radiative *LO*-phonon emission,[17] and the so-called thermal backfilling due to *LO*-phonon absorption from $|g_n\rangle$ to $|l_n\rangle$.[18] Although the form factors for the emission of photon and *LO*-phonon are different, both strongly depend on the overlap of wavefunctions between $|u_n\rangle$ and $|l_n\rangle$.[17] Hence, suppressing *LO*-phonon emission from the upper state comes at the cost of reducing the optical gain. Consequently, designs with higher f_{ul} (vertical designs) have shorter τ^u than those with a lower f_{ul} (diagonal designs). In diagonal designs, a higher carrier concentration (higher doping) can be used to compensate for the reduced optical gain. However, increasing the doping leads to an increase in $\Delta\nu$ due to the reduction of τ^u and T^* due to nonradiative elastic processes, including *e*–*e* and *imp* scattering. Therefore, the figure of merit $\frac{f_{ul}\tau^u}{\Delta\nu}$ appears to limit the performance of diagonal designs targeting high temperatures.[19]

Meanwhile, the escape of electrons to the continuum bands has been postulated as an unaccounted mechanism in THz QCLs for their temperature degradation.[20] To counteract the escape to the continuum, higher barrier compositions have been used in THz QCL designs.[16,20–23] To reduce the increased impact of *IFR* scattering—which scales quadratically with barrier composition—the number of barriers involved in electron transport should be minimized to reduce $\Delta\nu$. The most straightforward design in this direction is the so-called two-well scheme based on direct phonon depopulation, as illustrated in Fig. 1(b).[24,25]

Figure 1(c) shows the probability density functions of subband states in a THz QCL with a two wells scheme. Here, the injection barrier, radiation well, radiation barrier, and phonon well are labeled, i_b, r_w, r_b, and p_w respectively. Due to a shorter module length in this scheme, undesired coupling between neighboring modules may occur at the injection alignment, $|i_{n-1}\rangle \rightarrow |u_n\rangle$. The coupling between $|i_{n-1}\rangle$, $|u_n\rangle$ and the bound states in the neighboring modules, $|p_{1,n}\rangle$, $|p_{2,n}\rangle$, $|p_{1,n+1}\rangle$, and $|p_{2,n+1}\rangle$ was investigated, and by suppressing them, a record-high $T_{\max} = 250$ K was achieved.[16] The energy separation between $|i_{n-1}\rangle$ and $|p_{1,n}\rangle$ (denoted as $E_{i,pp}$) can be made arbitrarily high to reduce a possible leakage from $|i_{n-1}\rangle$ to $|p_{1,n+1}\rangle$.[16] However, as discussed in the supplementary material, the suppression of intermodule leakage (by increasing the $E_{i,pp}$) places an unfavorable upper limit on $f_{ul}\tau^u_{LO-em}$, where τ^u_{LO-em} is the lifetime due to nonradiative *LO*-phonon emission. In addition, if intermodule leakage is not suppressed, the transport simulations using a non-equilibrium Green function (NEGF) solver predicted results that substantially deviated from experiments.

In THz QCLs, a helpful graph to show the coupling between various channels is an anticrossing graph. An example of such a graph for several designs considered in this section is shown in Fig. 2(a). This graph shows the anticrossing curves over a wide range of module biases. Minima in the anticrossing correspond to a resonant alignment of two levels in energy, and the anticrossing gap is a measure of the coupling strength between those two levels. In an optimum scenario, the injection anticrossing (represented by the minima in the solid line) corresponding to alignment $|i_{n-1}\rangle \rightarrow |u_n\rangle$ should be close to the

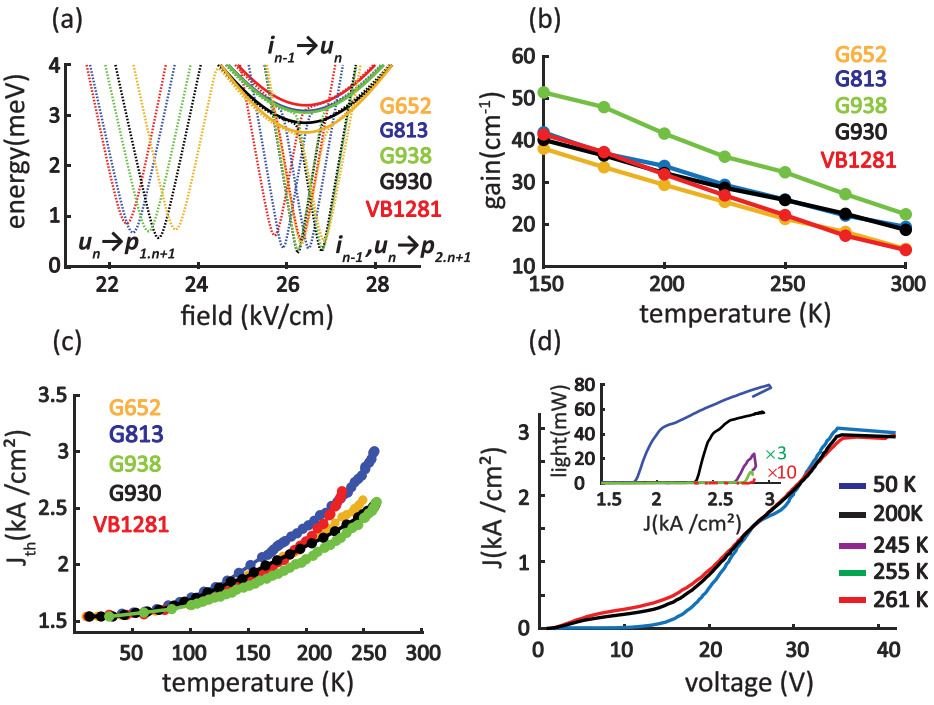

FIG. 2. (a) The anticrossing plot is employed for visually comparing different design proposals. A constant field is used to introduce a horizontal shift, ensuring alignment of biases at $|i_{n-1}\rangle \rightarrow |u_n\rangle$ for easier visual comparisons. (b) Simulated gain vs temperature using NEGF. (c) Experimentally measured $J_{th} - T$. The values of J_{th} from multiple devices are scaled to that of G652 at 10 K for easy comparison. (d) The voltage–current density–light characterization of G938. The sudden slope change in *L*–*J* relations at $T \leq 200$ K is due to detector saturation. The lasing frequency is ∼4 THz.

dephasing rate. The spontaneous emission's radiation linewidth is related to this dephasing rate. To estimate the linewidth, one can use Fourier transform infrared (FTIR) spectroscopy combined with step-scan techniques. This method results in an approximate value of 4 meV for the linewidth in terahertz quantum cascade lasers (THz QCLs).[26] It is crucial to highlight that this value does not directly correspond to the dephasing rate, and it may vary depending on factors, such as device design.[27] Therefore, it should be regarded as a general guideline rather than an absolute value. The transparency of the injection barrier ensures the minimum required doping to achieve population inversion and reduces the linewidth broadening due to *imp* scattering.[19] However, increasing the transparency of the injection barrier comes at the cost of an increase in the parasitic channels corresponding to the coalignment between $|i_{n-1}\rangle$, $|u_n\rangle$ and the bound states in the neighboring modules, $|p_{1,n}\rangle$, $|p_{2,n}\rangle$, $|p_{1,n+1}\rangle$, and $|p_{2,n+1}\rangle$ (minima in the dot lines).[16] Here, we optimized $\zeta = \frac{\Omega_{i_{n-1},u_n}}{\Omega_{u_n,p_{1,n+1}}}$ as a figure of merit to achieve both objectives. In semiconductor lasers, such as THz QCLs, the rate of increase in the threshold current density (J_{th}) with temperature carries information on the leakage into the parasitic channels.[17,20,28] In addition, $J_{\max} - T$ can be used to evaluate the transparency of the injection barrier. In a so-called lifetime limited transport, where the maximum current density through the injection barrier is limited by the upper state lifetime, $J_{\max}$ is temperature dependent. On the other hand, in tunneling-limited transport, the $J_{\max}$ is mainly limited by dephasing processes and is temperature-independent.[29,30] A slight decrease in $J_{\max}$ with temperature in diagonal designs indicates lifetime limited transport[31] and is sought after in this manuscript. The simulated gain vs temperature using NEGF is shown in Fig. 2(b) for these designs. The maximum operating temperature T_{max} can be inferred from Fig. 2(b), at which the gain decreases to the total cavity loss of ∼20 cm^{-1}.[32] This was corroborated by the temperature performance of G652 with $T_{max} \approx 250$ K.[16] Further details on the optimization scheme can be found in the supplementary material. A summary of growth parameters, the maximum operating temperature, and maximum and threshold current densities are summarized in Table I.

TABLE I. The layer sequence starts from the injection barrier. Bold denotes barriers separating GaAs quantum wells. The phonon well is indicated by parentheses, and the red ink indicates the doped region. The volume doping n_{3D} is defined relative to that of G652 (1.5×10^{17} cm^{-3}) and represented as n_{3D}^{G652} in the table. Here, x represents the aluminum fraction in the barriers. The number of modules is chosen for ∼10 μm of an active region.

Label	x (±0.003)	$T_{\max}$ (±0.1 k)	$J_{th}^{20K} - J_{\max}^{T_{\max}}$ (±20 A/cm^2)	Layer sequence (Å) (±.5 Å)	Doping
VB1281	0.25	232	1600–2650	**38.4**, 69.7, **24.2**, (27,25,93)	n_{3D}^{G652}
G813	0.3	260	1350–2600	**32.7**, 70.4, **20.8**, (57,30.57)	n_{3D}^{G652}
G930	0.35	259	1450–2700	**30.4**, 72.5,**19.1**, (59,28,59)	1.2 n_{3D}^{G652}
G902	0.35	260	2050–3350	**30.6** 73.0, **19.0**, (56,35,55)	1.2 n_{3D}^{G652}
G938	0.35	261	1750–2850	**28.8**, 74.5, **17.6**, (30,30,90)	n_{3D}^{G652}

A 25% Al barrier composition was used in VB1281 to reduce the impact of *IFR* scattering. As shown in Fig. 2(b), the NEGF simulations predict a similar gain in VB1281 compared to G652 with a $T_{max} = 250$ K.[16] The $T_{max} = 232$ K was achieved for this structure, the highest reported for designs based on 25% barriers (previously 210 K[21]) Since no drop of $J_{max} - T$ was observed in VB1281 (suggesting a tunneling transport regime), some improvements in T_{max} may still be possible using a higher ζ. However, as shown in Fig. 2(c), a higher rate of increase in $J_{th} - T$ in VB1281 was measured as compared to G652. This higher rate suggests thermal leakage to parasitic channels is more severe in 25% Al barriers and could explain the overestimation of gain in NEGF simulations.

In design that utilize 30% aluminum barriers, the T_{max} for G813 was improved to 260 K, aligning with recent theoretical predictions made by concurrent studies using a different implementation of the NEGF method.[23] Despite the superior operating temperature in G813, a higher rate of increase in $J_{th} - T$ is observed compared to G652, as shown in Fig. 2(c). Based on the anticrossing plot in Fig. 2(a) and the simulated subband population for G813 using the NEGF simulations shown in Fig. S7(d) of the supplementary material, there are no apparent leakage channels introduced compared to G652. Additionally, the regrowth of G813 exhibited the same behavior, indicating that growth problems can be ruled out. One possible explanation for the higher rate of increase in $J_{th} - T$ could be the $|l_n\rangle \rightarrow |p_{2,n+1}\rangle$ alignment. Further explorations are required to shed more light on the impact of this transport channel on the behavior of $J_{th} - T$. Though not shown here, the $J_{max} - T$ of G813 showed a negligible decrease with temperature, suggesting that the transport is tunneling limited and further reduction in injection barrier thickness and lower f_{ul} (a higher ζ) are worth pursuing. The details of this design labeled as VA1186-B are presented in the supplementary material. Another direction to improve the T_{max} of G813 is through doping scheme optimization, as explained in detail in the supplementary material.

In designs with 35% barriers, a similar temperature performance was measured in G930 as compared to G813, which is consistent with the NEGF simulations shown in Fig. 2(b). However, as shown in Fig. 2(c), the rate of increase in J_{th} with temperature is reduced in G930 compared to G813 and G652. This implies a higher suppression of thermal leakages. However, since G930 has a higher barrier composition, the *IFR* scattering rate might have been understated in our model for this barrier composition. Motivated by the simulated improvement of approximately 10 K in T_{max}, a design designated as G902 was explored. This design has an identical structure to G930, but with higher doping achieved through the same volume doping density (n_{3D}) and an expansion of the doped region by 1.2 times. However, even though G902 benefited from a higher growth quality compared to G930, no additional improvement was observed. The lack of gain improvement in G902 may be due to an underestimation of broadening caused by *imp* and *e–e* scattering in the simulation model. In G902, the measured J_{max} decreased from 3400 to 3350 A/cm^2 from 10 to 260 K suggesting the onset of a lifetime limited transport. As a result, further increase in ζ in this design was not pursued.

As discussed in the supplementary material, designs with a wider phonon-well have a higher value of the figure of merit $f_{ul}\tau^{u}_{LO-em}$ and show a higher gain in the simulations—however, designs based on this resulted in an unfavorable fast increase in $J_{th} - T$. In G938, we explored the possibility of a wider phonon-well than G930. This design also has a similar ζ as G813, which makes the comparison with the 30% designs easier. The doping position was also optimized in G938 using the model explained in the supplementary material file. As shown in Fig. 2(b), the simulated gain in G938 is higher than G930 when the same statistical parameters are used to describe the interface. However, the T_{max} was not improved as much as expected. The rate of $J_{th} - T$ in G938 did not increase as compared to G930, in contrast to the trend observed in 30% barriers for wider phonon wells. Two possible experimental factors may have hindered the performance of G938 in comparison to simulation predictions. First, the fabrication of G938 encountered several issues, and only the edge pieces of the wafer were used for characterization. In our previous experiments, we have observed an improvement of approximately 5–10 K when using central pieces compared to edge pieces. Second, the MBE growth quality of G938 was inferior to that of G930, as evidenced in the supplementary material. A future regrowth of this wafer may verify if the improvement predicted by the simulation for G938 compared to G930 can be realized experimentally. The measured voltage–current–light for G938 is shown in Fig. 2(d). The maximum current density in G938 is reduced from 3000 A/cm^2 at 10 K to 2850 A/cm^2 at 261 K. Given the results, further increase in ζ in this design was not pursued. However, it is worth investigating the potential benefits of co-aligning $|l_n\rangle \rightarrow |p_{2,n+1}\rangle$ and $|i_{n-1}\rangle \rightarrow |u_n\rangle$ in designs with 35% barriers to determine if this double depopulation scheme can lead to a higher gain.

Thus far, the investigation has revealed that intermodule leakage imposes various restrictions on the two-wells scheme. To alleviate these constraints, one potential solution is to utilize direct phonon depopulation with multiple injector wells. As shown in Fig. 3(a), an example of such a design with two injectors $^1i_{n-1}$ and $^2i_{n-1}$ is presented. For ease of reference, we refer to this design as the three-well scheme. From a simulation perspective, with the same barrier composition, an optimized three-well scheme has lower gain compared to an optimized two-well design. This can be explained by the fact that the three-well scheme requires higher doping to reach the same J_{max}, due to its longer module length, which leads to greater gain broadening. Additionally, with more barriers involved in injecting carriers into the upper lasing level, this scheme also experiences higher dephasing from IFR scattering. Despite these drawbacks, there are still two significant potential benefits to exploring three-well schemes. From a transport simulation perspective, it was predicted that room temperature operation could be achieved by reducing the injection barrier thickness and increasing doping (higher J_{max}) in designs, such as VB1281 and G813. However, these predictions were not experimentally realized. In other words, if the simulation assumptions are more accurate in a three-well scheme due to reduced intermodule leakages, then its simulated maximum operating temperature (T_{max}) will be closer to the experimental results compared to the two-well designs, even though the latter may have a higher predicted gain. If the maximum operating temperature of G813 was limited by the trade-off between the transparency of the injection barrier and intermodule leakage, a three-well scheme with a similar injection barrier thickness that leads to the same J_{th} and J_{max} should, in theory, show a lower rate of increase in $J_{th} - T$ compared to G813. In this scenario, the design direction would be to gradually reduce the thickness of injection barriers to achieve a higher gain than G813. With this approach in mind, a three-well design labeled G936 was explored.

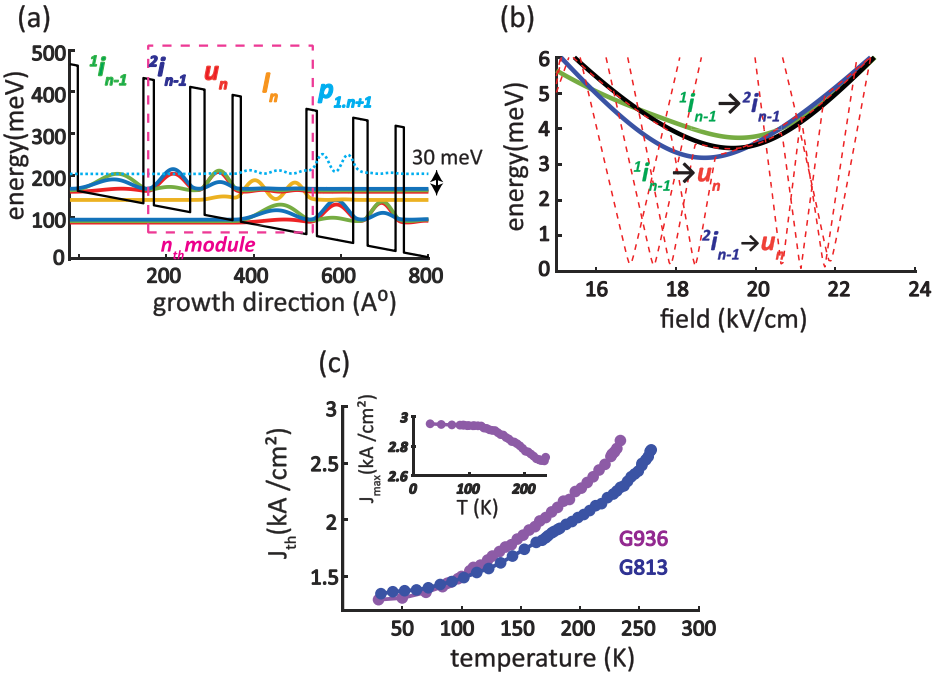

FIG. 3. (a) Probability density functions of subband states in a THz QCL with two injectors and direct phonon depopulation. (b) Anticrossing graph for G936. The growth parameters starting from the injection barrier are **33**, 64.3, **19**, (59, 29, 59), **24**, and 83.3. The bold font indicates barriers, and the red ink indicates the doped region with $n_{3D} = 1.7 \times 10^{17}$ cm^{-3}. The number of modules is chosen for ∼10 μm of the active region. (c) Comparing experimentally measured $J_{th} - T$ between G813 and G936 and $J_{max} - T$ for G936 as inset. Both designs have a lasing frequency of ∼4 THz.

The anticrossing graph for G936 is shown in Fig. 3(b). The $J_{th} - T$ with $J_{max} - T$ as inset for G936 is plotted in Fig. 3(c). G936 achieved approximately the same J_{th} as G813, and reached $T_{max} = 235\,K$, the highest reported T_{max} for a three-well scheme to this date (previously 200 K[33]). However, the $J_{th} - T$ shows a faster increase compared to G813. The drop of $J_{max} - T$ suggests that this design is lifetime limited, and the higher increasing rate of $J_{th} - T$ suggests thermal leakage. Further exploration is needed to investigate the impact of possible parasitic channels such as $|p_{n+1}\rangle$ that has a smaller energy separation (∼30 meV) with injector doublet [Fig. 3(a)] than that in G813. More importantly, a systematic study is required to investigate if a reduction in *IFR* scattering in three-well schemes with reduced barrier composition (such as 25%) can offer advantages compared to the two-well schemes with barriers ≥ 30%.

In conclusion, we achieved T_{max}= 261 K for THz quantum cascade lasers. To further improve the temperature performance, optimizing the growth conditions to reduce defects at the interface might be necessary, given the requirement for higher barrier compositions to suppress parasitic channels.

See the supplementary material for a comprehensive overview of the non-equilibrium green function model; tradeoffs in the direct phonon depopulation scheme; the gain optimization procedure; the effect of the doping profile; molecular beam epitaxy (MBE) growth; characterization methods; and twelve figures and two tables for reference, crucial for fully comprehending the content and scope of the main manuscript.

This work was supported by the National Science Foundation (NSF). This work was performed, in part, at the Center for Integrated Nanotechnologies, an Office of Science User Facility operated for the U.S. Department of Energy, Office of Science. Sandia National Laboratories is a multimission laboratory managed and operated by National Technology and Engineering Solutions of Sandia, LLC, a wholly owned subsidiary of Honeywell International, Inc., for the U.S. Department of Energy's National Nuclear Security Administration under Contract No. DE-NA0003525. This paper describes objective technical results and analysis. Any subjective views or opinions that might be expressed in the paper do not necessarily represent the views of the U.S. Department of Energy or the United States Government. The work at University of Waterloo was supported in part by Canada First Research Excellence Fund and the Natural Sciences and Engineering Research Council of Canada (NSERC).

We would like to thank nextnano GmbH for providing an evaluation license, which has been invaluable in our work. We also want to acknowledge the earlier attempts of Dr. Asaf Albo on the three-well scheme that yielded a T_{max} ∼ 170 K in 2017.

AUTHOR DECLARATIONS

Conflict of Interest

The authors have no conflicts to disclose.

Author Contributions

Ali Khalatpour and Man Chun Tam contributed equally to this work.

Ali Khalatpour: Conceptualization (equal); Investigation (equal); Writing – original draft (equal). **Man Chun Tam:** Investigation (equal). **Sadhvikas Addamane:** Investigation (equal). **John L. Reno:** Investigation (equal). **Zbignew R. Wasilewski:** Investigation (lead). **Qing Hu:** Funding acquisition (lead); Investigation (lead); Supervision (lead).

DATA AVAILABILITY

The data that support the findings of this study are available within the article and its supplementary material.

REFERENCES

[1]J. V. Siles, K. B. Cooper, C. Lee, R. H. Lin, G. Chattopadhyay, and I. Mehdi, "A new generation of room-temperature frequency-multiplied sources with up to 10× higher output power in the 160-GHz–1.6-THz range," IEEE Trans. THz. Sci. Technol. **8**, 596–604 (2018).

[2]I. Mehdi, J. V. Siles, C. Lee, and E. Schlecht, "THz diode technology: Status, prospects, and applications," Proc. IEEE **105**, 990–1007 (2017).

[3]P. Chevalier, A. Amirzhan, F. Wang, M. Piccardo, S. G. Johnson, F. Capasso, and H. O. Everitt, "Widely tunable compact terahertz gas lasers," Science **366**, 856–860 (2019).

[4]M. A. Belkin, F. Capasso, A. Belyanin, D. L. Sivco, A. Y. Cho, D. C. Oakley, C. J. Vineis, and G. W. Turner, "Terahertz quantum cascade laser source based on intracavity difference-frequency generation," Nat. Photonics **1**, 288–292 (2007).

[5]Q. Lu, N. Bandyopadhyay, S. Slivken, Y. Bai, and M. Razeghi, "Continuous operation of a monolithic semiconductor terahertz source at room temperature," Appl. Phys. Lett. **104**, 221105 (2014).

[6]L. Li, L. Chen, J. Freeman, M. Salih, P. Dean, A. Davies, and E. Linfield, "Multi-Watt high-power THz frequency quantum cascade lasers," Electron. Lett. **53**, 799–800 (2017).

[7]Y. Jin, J. L. Reno, and S. Kumar, "Phase-locked terahertz plasmonic laser array with 2 W output power in a single spectral mode," Optica **7**, 708–715 (2020).

[8]L. Li, L. Chen, J. Zhu, J. Freeman, P. Dean, A. Valavanis, A. Davies, and E. Linfield, "Terahertz quantum cascade lasers with >1 W output powers," Electron. Lett. **50**, 309–311 (2014).

[9]A. Khalatpour, J. L. Reno, and Q. Hu, "Phase-locked photonic wire lasers by π coupling," Nat. Photonics **13**, 47–53 (2019).

[10]A. Khalatpour, J. L. Reno, N. P. Kherani, and Q. Hu, "Unidirectional photonic wire laser," Nat. Photonics **11**, 555–559 (2017).

[11]D. Burghoff, T.-Y. Kao, N. Han, C. W. I. Chan, X. Cai, Y. Yang, D. J. Hayton, J.-R. Gao, J. L. Reno, and Q. Hu, "Terahertz laser frequency combs," Nat. Photonics **8**, 462–467 (2014).

[12]M. Rösch, G. Scalari, M. Beck, and J. Faist, "Octave-spanning semiconductor laser," Nat. Photonics **9**, 42–47 (2015).

[13]T.-Y. Kao, J. L. Reno, and Q. Hu, "Amplifiers of free-space terahertz radiation," Optica **4**, 713–716 (2017).

[14]C. Walker, C. Kulesa, A. Young *et al.*, "Gal/Xgal U/LDB spectroscopic/stratospheric THz observatory: GUSTO," in *Millimeter, Submillimeter, and Far-Infrared Detectors and Instrumentation for Astronomy XI* (SPIE, 2022), Vol. 12190.

[15]A. Khalatpour, A. K. Paulsen, S. J. Addamane, C. Deimert, J. L. Reno, Z. R. Wasilewski, and Q. Hu, "A tunable unidirectional source for GUSTO's local oscillator at 4.74 THz," IEEE Trans. THz. Sci. Technol. **12**, 144–150 (2022).

[16]A. Khalatpour, A. K. Paulsen, C. Deimert, Z. R. Wasilewski, and Q. Hu, "High-power portable terahertz laser systems," Nat. Photonics. **15**, 16–20 (2021).

[17]J. Faist, *Quantum Cascade Lasers* (Oxford University Press, Oxford, 2013).

[18]B. S. Williams, H. Callebaut, S. Kumar, Q. Hu, and J. L. Reno, "3.4 THz quantum cascade laser based on LO-phonon scattering for depopulation," Appl. Phys. Lett. **82**, 1015 (2003).

[19]C. W. I. Chan, A. Albo, Q. Hu, and J. L. Reno, "Tradeoffs between oscillator strength and lifetime in terahertz quantum cascade lasers," Appl. Phys. Lett. **109**, 201104 (2016).

[20]A. Albo, Y. V. Flores, Q. Hu, and J. L. Reno, "Two-well terahertz quantum cascade lasers with suppressed carrier leakage," Appl. Phys. Lett. **111**, 111107 (2017).

[21]L. Bosco, M. Franckié, G. Scalari, M. Beck, A. Wacker, and J. Faist, "Thermoelectrically cooled THz quantum cascade laser operating up to 210 K," Appl. Phys. Lett. **115**, 010601 (2019).

[22]B. Wen and D. Ban, "High-temperature terahertz quantum cascade lasers," Prog. Quantum Electron. **80**, 100363 (2021).

[23]V. Rindert, E. Önder, and A. Wacker, "Analysis of high-performing terahertz quantum cascade lasers," Phys. Rev. Appl. **18**(4), L041001 (2022).

[24]S. Kumar, C. W. I. Chan, Q. Hu, and J. L. Reno, "Two-well terahertz quantum-cascade laser with direct intrawell-phonon depopulation," Appl. Phys. Lett. **95**, 141110 (2009).

[25]G. Scalari, M. I. Amanti, C. Walther, R. Terazzi, M. Beck, and J. Faist, "Broadband THz lasing from a photon–phonon quantum cascade structure," Opt. Express **18**, 8043–8052 (2010).

[26]B. S. Williams, "Terahertz quantum cascade lasers," Ph.D. dissertation (Massachusetts Institute of Technology, 2003).

[27]S. Kumar and Q. Hu, "Coherence of resonant-tunneling transport in terahertz quantum-cascade lasers," Phys. Rev. B **80**, 245316 (2009).

[28]H. Page, C. Becker, A. Robertson, G. Glastre, V. Ortiz, and C. Sirtori, "300-K operation of a GaAs-based quantum-cascade laser at $\lambda \approx 9\,\mu$m," Appl. Phys. Lett. **78**, 3529–3531 (2001).

[29]R. Köhler, R. C. Iotti, A. Tredicucci, and F. Rossi, "Design and simulation of terahertz quantum cascade lasers," Appl. Phys. Lett. **79**, 3920–3922 (2001).

[30]H. Callebaut and Q. Hu, "Importance of coherence for electron transport in terahertz quantum cascade lasers," J. Appl. Phys. **98**, 104505 (2005).

[31]I. Bhattacharya, C. W. I. Chan, and Q. Hu, "Effects of stimulated emission on transport in terahertz quantum cascade lasers based on diagonal designs," Appl. Phys. Lett. **100**, 011108 (2012).

[32]D. Burghoff, T. Yu. Kao, D. Ban, A. W. M. Lee, Q. Hu, and J. Reno, "A terahertz pulse emitter monolithically integrated with a quantum cascade laser," Appl. Phys. Lett. **98**, 061112 (2011).

[33]S. Fathololoumi, E. Dupont, C. Chan, Z. Wasilewski, S. Laframboise, D. Ban, A. Mátyás, C. Jirauschek, Q. Hu, and H. Liu, "Terahertz quantum cascade lasers operating up to ∼200 K with optimized oscillator strength and improved injection tunneling," Opt. Express **20**, 3866–3876 (2012).